NiMo Solid Solution Nanowire Array Electrodes for Highly Efficient Hydrogen Evolution Reaction

Adeela Nairan, Peichao Zou, Caiwu Liang, Jiaxing Liu, Dang Wu, Peng Liu, and Cheng Yang*

Developing high-performance noble metal–free electrodes for efficient water electrolysis for hydrogen production is of paramount importance for future renewable energy resources. However, a grand challenge is to tailor the factors affecting the catalytic electrodes such as morphology, structure, and composition of nonprecious metals. Alloying catalytic metals can lead to a synergistic effect for superior electrocatalytic properties. However, alloy formation in solution at low synthesis temperatures may result in better catalytic properties as compared to those at high temperatures due to the controlled reaction kinetics of nucleation and growth mechanisms. Herein, an aqueous solution–based preparation technology is developed to produce NiMo alloy nanowire arrays. The NiMo alloy shows significantly improved hydrogen evolution reaction (HER) catalytic activity, featured with extremely low overpotentials of 17 and 98 mV at 10 and 400 mA cm^{-2}, respectively, in an alkaline medium, which are better than most state-of-the-art non-noble metal–based catalysts and even comparable to platinum-based electrodes. Analyses indicate that the lattice distortions induced by Mo incorporation, increased interfacial activity by alloy formation, and plenty of MoNi$_4$ active sites at nanowires surface collectively contribute to remarkably enhanced catalytic activity. This study provides a powerful toolbox for highly efficient nonprecious metal–based electrodes for practical HER application.

1. Introduction

Electrocatalytic splitting of water is an eco-friendly approach for scalable production of clean hydrogen (H$_2$) energy.[1] Noble metal-based electrodes are the most active catalysts for hydrogen evolution reaction (HER); however, high cost and scarcity impede the global scale implementation.[2] Therefore, it remains a crucial challenge to design cost-effective and earth-abundant electrocatalysts with improved catalytic activity for mass production. Regarding the earth abundance, high electrical conductivity, high corrosion resistance, and outstanding durability, Ni-based electrocatalysts have been reported as potential candidates for hydrogen production in alkaline medium.[3] In order to improve electrocatalytic activity, doping/alloying Ni with other nonprecious metals has been employed, which can modulate its electronic structure and significantly improve the electrocatalytic activity, and thus compensate the disadvantages of solely using pure Ni.[3a] Among them, NiMo alloy based catalysts have been regarded as one of the most promising candidates in alkaline conditions, as Ni atoms have strong water dissociation ability and Mo atoms possess superior H$_2$ adsorption ability, and thus their alloys can enable more effective H$_2$ chemisorption with optimized value of hydrogen binding energy in a synergistic manner.[4] However, due to the large reduction potential difference between these two metals, it is quite challenging to employ coreduction method to produce NiMo alloy at low synthesis temperature, and most of the available preparation methods are still metallurgical ones. Yet, a high-temperature fabrication process can lead to annealing of metal, which is unfavorable for remaining more surface-active sites as well as a high specific surface area, which are both critically important for electrocatalysis.[5] Thus, developing a scalable and reproducible low-temperature alloy electrode fabrication method is significantly urgent and critical, which can preserve ample reactive sites as well as high specific surface area for better catalytic performance. In this regard, Zhang et al. attempted to fabricate NiMo nanosheet arrays constructed on Ni foam via a coprecipitation-thermal reduction at 180 °C, which is much lower than their melting points. The prepared catalyst requires an overpotential of 35 mV to approach a current density of 10 mA cm^{-2} for HER,[6] which is comparable to the commercially available Pt/C catalyst. Hou et al. fabricated a core–shell architecture of nitrogen-doped carbon sheath through hydrothermal synthesis of NiMo@NiMoO$_x$ nanowires at 150 °C for 6 h, followed by growing nitrogen-doped carbon sheath (NC) at 400 °C (NC@NiMo@NiMoO$_x$). The fabricated electrode requires an overpotential of 29 mV to approach a current density of 10 mA cm^{-2} for HER in alkaline medium.[7] Yet, comparing with the state-of-the-art

Dr. A. Nairan, Dr. P. Zou, C. Liang, J. Liu, Dr. D. Wu, P. Liu, Prof. C. Yang
Division of Energy and Environment
Graduate School at Shenzhen
Tsinghua University
Shenzhen 518055, China
E-mail: yang.cheng@sz.tsinghua.edu.cn

Pt-based catalysts (overpotential less than 20 mV to reach current density of 10 mA cm^{-2}),[8] further enhancing the electrocatalytic performance of NiMo-based electrodes is still challenging and urgently needed.

Other than turning the knob on elemental doping of catalyst, enormous efforts have been made to push up the HER performance of the catalytic electrode beyond the limitation determined by the geometry of a specific catalyst particle in a regular case of randomly dispersed on a reticular conductive scaffold. In this regard, constructing 3D nanostructured electrodes with intrinsically catalytic-active surface species has been regarded as an effective strategy featured with large surface area, excellent mechanical stability, and efficient mass/charge transfer and gas escaping through the entire electrode architecture.[9] In many cases along with self-organized hierarchical nanostructures, growth of nanomaterials on templates (such as anodized aluminum oxide based hard-template and organic molecules based soft-template) has been intensively studied.[10] However, these template-assisted synthesis procedures provide less electrochemical active sites and poor mass transfer due to the smooth template surface and limited particle size for nanostructures growth. Additionally, after removing the templates, the as-obtained nanostructures can easily get agglomerated.[11] Moreover, most available methods are difficult to reduce costs by scaling up to industrial fabrication. As compared, a more ideal situation is to develop self-standing hierarchical nanostructures with interconnected micro/nanochannels for electrode material due to their macrodimensional characteristic and mechanical integrity. Among all available geometries, hierarchical nanowire array electrode is of primary interest which provides sufficient number of active sites and fast charge transfer process. Another advantage of such electrodes is the mechanical and chemical stability that can endure the long-term reaction kinetics of electrodes.[12] Yet, the fundamental challenge is to fabricate electrode with excellent reaction kinetics through a facile and cost-effective method for large-scale application.

By taking above challenges into account, here in this work, we report an aqueous-solution based synthesis of NiMo solid solution nanowire array electrode with superior HER performance. By rationally designing the composition, morphology, and structural characteristics, the catalyst electrode was fabricated in a scalable and low-cost manner, featured with a uniform magnetic field assisted growth mechanism, with the nanowires vertically grafted on titanium substrate by metallurgical bond, forming uniform arrays up to decimeter size (Figure S1, Supporting Information). This method requires short reaction time and low temperature in comparison with conventional methods where high temperature and a long time are necessary.[6,7,13] Interestingly, NiMo alloy is randomly distributed in the Ni nanowires during one-step growth process. This integrated 3D hierarchical structure of NiMo alloy on Ni nanowires shows excellent electrical conductivity, high density of catalytic active sites, and superior charge/mass transport and hydrogen bubbles abilities. The electrode exhibits enhanced composition-dependent catalytic activity and electrochemical stability, with the lowest overpotential of 17 mV at a current density of 10 mA cm^{-2} and a small Tafel slope of 28 mV dec^{-1}, which is better than commercially available Pt/C catalyst and even comparable to the state-of-the-art Pt-based catalysts.

2. Results and Discussion

2.1. Preparation and Structural Characterization of NiMo-Based Electrodes

NiMo solid solution nanowire arrays were synthesized by a facile magnetic field assisted growth process as illustrated in **Figure 1**a. In this work, NiMo composition and the growth temperature have been considered two crucial factors to fabricate high-performance NiMo-based electrode. The experiments were initially designed with different weight ratios of NiCl$_2$·6H$_2$O to Na$_2$MoO$_4$·2H$_2$O with 95:05, 90:10, and 80:20 while the growth temperature was kept constant at 80 °C. Among, NiMo electrode with 5 wt% Mo salt exhibits the highest electrochemical performance (Figure 3a) and was reconsidered to fabricate a series of controlled temperature dependent experiments. It has been noticed that NiMo electrode (5 wt% Mo salt) fabricated at 65 °C (named as NiMo-65) represented excellent catalytic performance (Figure 3c). The detail of electrode fabrication is elucidated in the Experimental Section.

The morphology of prepared NiMo electrodes was first interrogated by using scanning electron microscopy (SEM). Figure 1b depicts the uniform growth of NiMo-65 with nanowire length of 860 μm (Figure S2, Supporting Information). The vertically aligned nanowires possess uniform morphology distribution, large surface area, and provide fast electron transfer to the active sites for HER. In contrast, the significant change in morphology was observed for the electrode prepared at other compositions (Figure S3, Supporting Information) and synthesis temperatures (Figure S4, Supporting Information). It was found that the nanowire geometry with a length up to 860 ± 50 μm can be achieved between 80 and 65 °C; however, under a lower synthesis temperature (60 °C), only nanochain-like structure can be obtained. After further decreasing the synthesis temperature (50 °C), it only shows formation of nanoparticles with decreased growth rate (Figure S4, Supporting Information). The average calculated diameters of the as-prepared samples with respect to different synthesis temperatures are plotted in Figure S5 (Supporting Information). The above results indicate that by controlling the growth temperature, different morphologies can be obtained.

To obtain more insight into the structural and morphological details, transmission electron microscopy (TEM) images were studied. Figure 1c represents the selected area diffraction pattern (SAED) of the fabricated NiMo-65 nanowires, where the diffraction rings are well indexed to the corresponding planes of Ni metal. From the TEM image of NiMo-65 nanowires (Figure 1d), clear step sites/kinks can be identified on the nanowire surface. From geometric point of view, when the diameter of nanowire narrows down, there will be more atoms exposed on the corners/edges,[14] which can contribute to improve the catalytic activity. Figure 1e displays the high-resolution TEM (HRTEM) image of the NiMo-65 sample, and further details of its structure are obtained from fast Fourier transform (FFT) patterns and inverse fast Fourier transform (IFFT) patterns (Figure 1f,g) of the selected areas marked in Figure 1e, which confirms the fcc phase of Ni. Figure 1g shows lattice fringes with distance of 0.203 nm, corresponding to the (111) plane of Ni metal. However, Figure 1f reveals the lattice
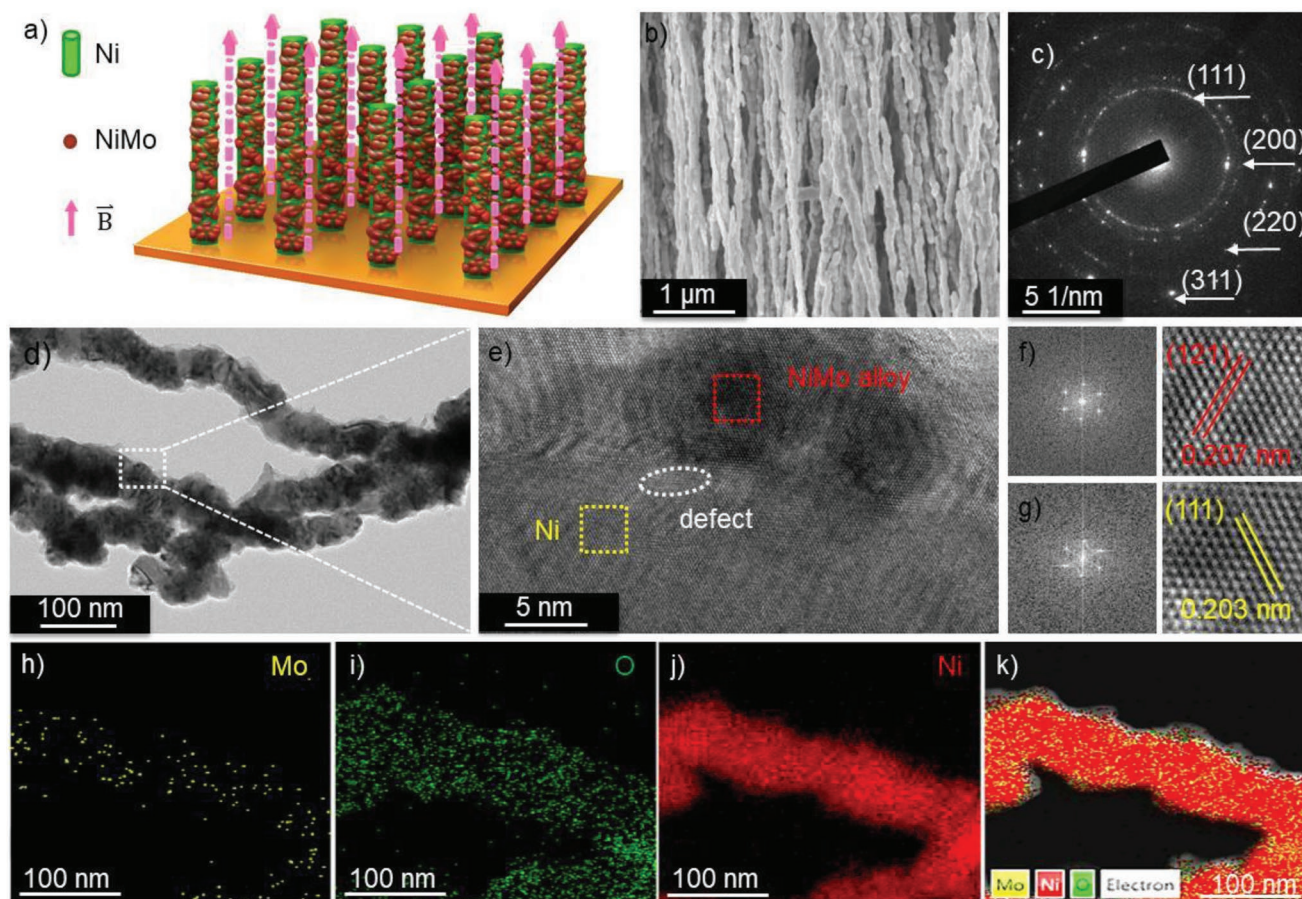
Figure 1. a) Schematic illustration of fabrication of NiMo nanowire arrays through magnetic field assisted growth process, where dotted lines represent the magnetic field lines. b) SEM image of NiMo-65 electrode. c) SAED pattern of NiMo-65 electrode. d) TEM image of NiMo-65 electrode. e) HRTEM image of NiMo-65. f) FFT and IFFT pattern of top region highlighted in (e). g) FFT and IFFT pattern of region highlighted at the bottom of (e). h–k) EDS elemental mapping of Mo, O, Ni, and integrated elemental mapping image.

fringe spacing of 0.207 which corresponds to the (121) facet of MoNi$_4$ alloy, suggesting the formation of NiMo alloy (JCPDS No. 65-5480) with the morphology of nanodots anchored on the Ni nanowires (Figure 1e). Figure 1e clearly displays formation of NiMo alloy along with a great deal of lattice mismatch or surface defects. In contrast, such defective characteristic can hardly be observed in HRTEM image of NiMo samples with different Mo incorporation (1.60, 0%) prepared at 80 °C (Figures S6b and S7c, Supporting Information). The detailed TEM analysis of sample prepared with 0% Mo incorporation is shown in Figure S7 (Supporting Information). The above results demonstrate that degree of disorder can be controlled by simply varying the synthesis temperature and this factor can also contribute to HER catalytic activity. The elemental mapping of the NiMo-65 electrode shows homogenous distribution of Ni with granular distribution of Mo on the surface of nanowire, while O comes from atmosphere during performing the measurement (Figure 1h–j). The integrated image of the nanowire corroborated the granular distribution of Mo on the nanowire surface (Figure 1k). Furthermore, the corresponding energy-dispersive X-ray spectroscopy (EDX) confirms that the atomic ratio of Ni and Mo in nanowire is 98.22:1.78 (Figure S8, Supporting Information).

The crystalline nature of the as-prepared solid solution nanowire arrays was confirmed by X-ray diffraction (XRD). **Figure 2**a represents the XRD patterns recorded for NiMo electrode samples with different Mo content synthesized at 80 °C. The diffraction peaks located at 2θ ≈ 44.6°, 52.0°, and 76.6° are assigned to the (111), (200), and (220) Ni facets, respectively (JCPDS No. 04-0850). Noticeably, there is no obvious peak for MoNi$_4$ alloy due to the small actual Mo concentration measured from inductive coupled plasma (ICP) spectroscopy (Table S1, Supporting Information). The obtained Mo concentration in NiMo nanowire arrays was found to be Mo = 1.60, 2.63, and 2.85 at% for Ni and Mo precursor ratios of 95:05, 90:10, and 80:20, respectively. However, diffraction peaks shifted toward the lower 2θ values, which can be attributed to the lattice expansion due to successful incorporation of Mo into Ni.[15] The strain induced by the lattice expansion has been calculated from XRD pattern and listed in Table S2 (Supporting Information). XRD patterns for NiMo (1.60 at% Mo) electrodes prepared at different temperatures are shown in Figure 2b. Clearly, decrease in crystallinity was observed for the samples synthesized at 65 °C. This decrease can be attributed to the increased number of surface defects such as lattice strain, kinks, and corresponding increase in active sites. The obtained
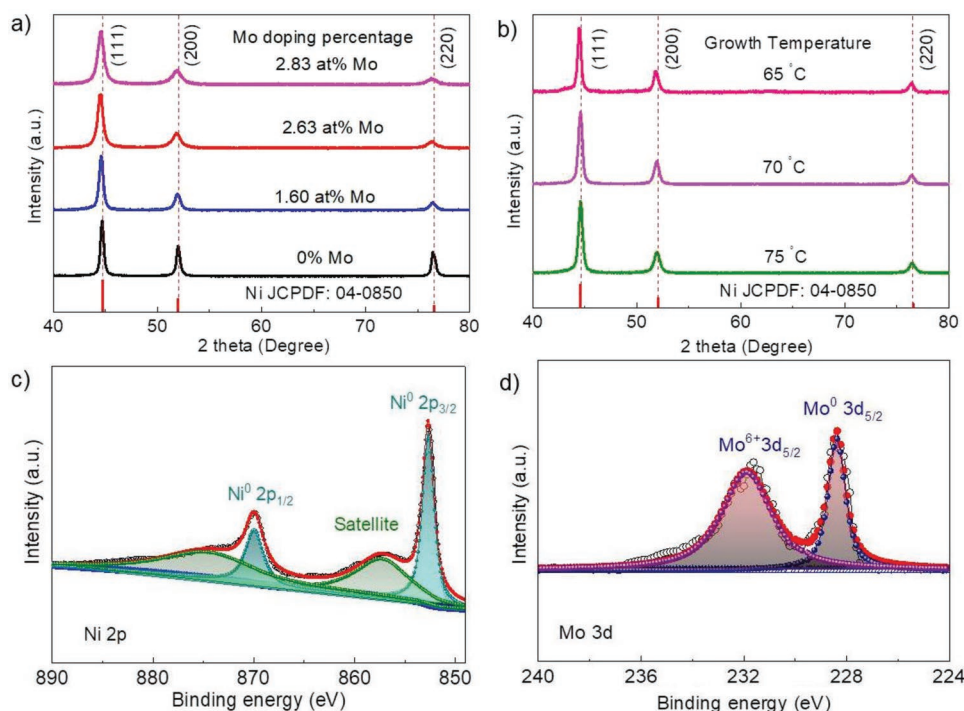
Figure 2. a) XRD pattern of NiMo-based electrodes prepared at 80 °C with different Mo content. b) XRD pattern of NiMo-based electrodes (1.60 at% Mo) prepared at different synthesis temperatures. c,d) High-resolution XPS spectra of NiMo-65 for Ni 2p and Mo 3d.

data reveal that reaction temperature plays a vital role for surface engineering of active sites, which resultantly boost up the electrochemical activity of the electrode.

In consideration of the hierarchical NiMo electrodes, specific surface area of the prepared electrode was investigated by Brunauer–Emmett–Teller (BET) technique. N_2 adsorption–desorption isotherms (Figure S9, Supporting Information) show that the NiMo-65 electrode has a specific surface area of 35 m^2 g^{-1}, which is a very high value for metal-based porous materials for electrocatalysis application. BET analysis indicates the formation of open-porous nanowire arrays structure; this aligned and reticular structure facilitates the transport of electrolyte through the whole architecture and fast release of gases from the surface.

To further confirm the chemical composition and electronic states of the prepared nanowire arrays electrode, X-ray photoelectron spectroscopy (XPS) investigation was conducted. Figure 2c,d represents the XPS spectra of NiMo-65 electrode for Ni 2p and Mo 3d, respectively. Ni 2p spectrum shows two main peaks at 852.6 and 869.5 eV, accompanied by two broad satellite peaks, which correspond to metallic Ni.[16] While, in case of Mo 3d spectrum, the prominent peak appearing at 227.9 eV can be indexed to metallic Mo,[17] and the peak located at 232 eV is referred to the Mo^{6+} state. The appearance of oxidized state of Mo can be attributed to the superficial oxidation of Mo species when exposed to ambient atmosphere for characterizations.[18] Quantitative analysis shows a Ni/Mo atomic percentage is ≈98.4:1.60, which corroborates well with ICP and TEM results. Furthermore, the XPS spectrum for the NiMo sample prepared at 80 °C is shown in Figure S10 (Supporting Information), which also confirms the presence of mixed valence states

of metal ions. The XPS survey scan spectrum recorded for NiMo-65 is shown in Figure S11 (Supporting Information), which confirms the existence of Ni, Mo, and O. The deconvolution spectra for O1s and C1s arising from NiMo are shown in Figure S12 (Supporting Information), respectively. To further confirm the structural evolution, Raman spectrum of NiMo electrode was studied (Figure S13, Supporting Information). The obtained spectrum did not show any strong characteristic peak related to the oxidized state of Ni and Mo, showing dominance of metallic phases in as-prepared NiMo nanowires. Therefore, the combined analyses of TEM, XPS, and Raman indicate the formation of NiMo alloy integrated on the Ni nanowires.

2.2. Electrocatalytic HER Performance

The HER activity of the NiMo-based electrodes and benchmarking commercially available 20% Pt/C catalyst was evaluated in 1.0 M KOH solution, using a three-electrode setup with Ag/AgCl electrode and graphite rod as the reference and counter electrode, respectively. **Figure 3**a shows the linear sweep voltammetry (LSV) curves of NiMo electrodes fabricated at 80 °C with different Mo compositions, after iR compensation. For comparison, the LSV curves for bare Ti substrate and Pd electroplated Ti substrate are shown in Figure S14 (Supporting Information). As can be seen, at a current density of 10 mA cm^{-2}, the lowest overpotential of 34 mV was achieved for NiMo electrode with 1.60 at% Mo, which was comparable to the commercially available Pt/C catalyst (45 mV), and much lower than those of NiMo electrodes with 0 at%
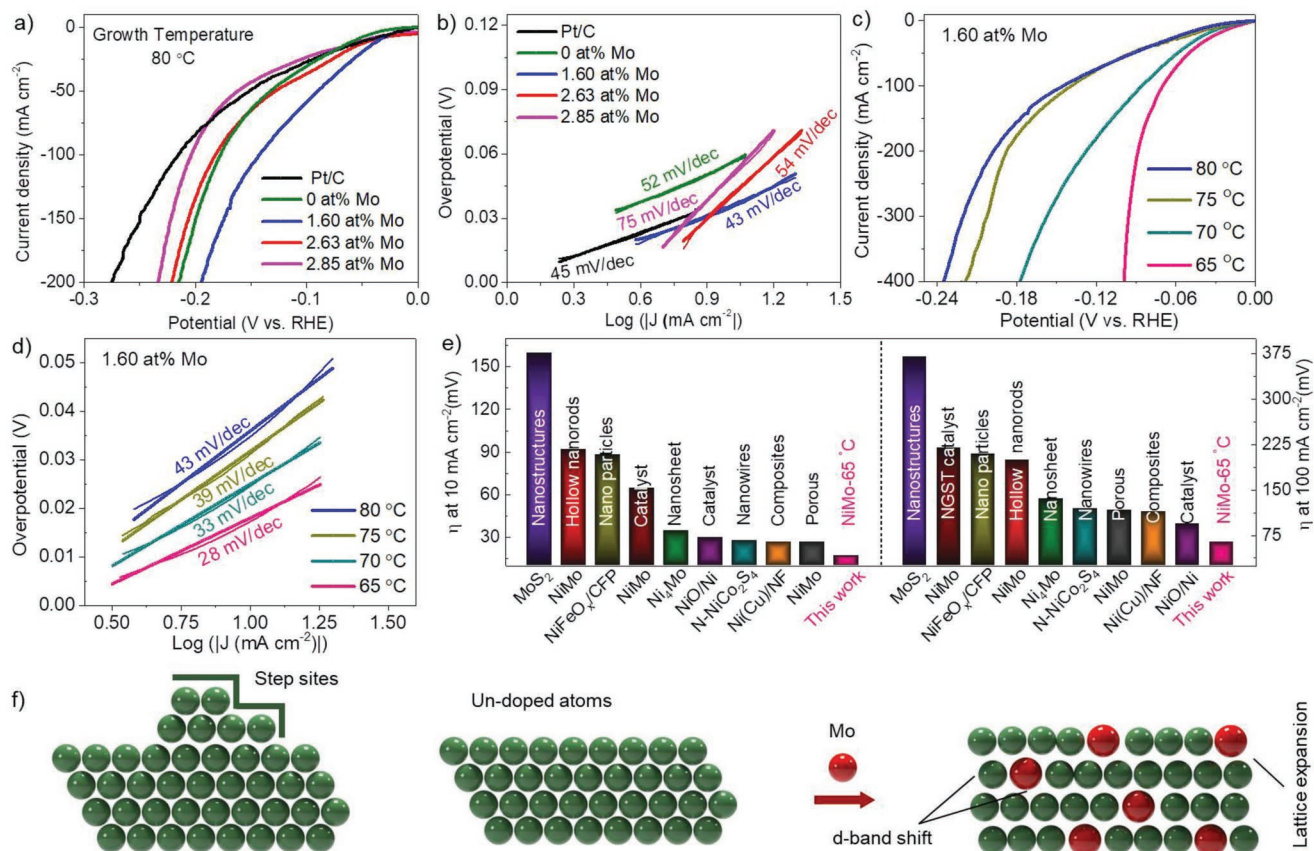
Figure 3. a) LSV curves for NiMo-electrode prepared at 80 °C with different at% of Mo and b) corresponding Tafel plots. c) LSV curves of NiMo-electrode (1.60 at% Mo) synthesized at different temperatures and d) corresponding Tafel plots. e) Comparison of the overpotentials of NiMo-65 electrode and other recently reported catalysts at current densities of 10 and 100 mA cm^{-2} in 1.0 M KOH aqueous solution. f) Schematic representation of structural features of NiMo-65.

Mo (56 mV), 2.63 at% Mo (40 mV), and 2.85 at% Mo (48 mV). These results show a monotonic trend in which increase in Mo resulted in decreased catalytic activity, along with a transformed morphology from kinked shape to spherical/smooth nanowire surface (Figure S2, Supporting Information). Similar behavior with Mo incorporation has been observed in previous reports, which confirms that controlled material concentration can significantly promote the catalytic activity,[15a,19] as it preserves a good control of morphology (as discussed in SEM). The improved HER activity of NiMo-based electrodes can also be achieved due to the synergistic effects between Ni and Mo, as Ni atoms are fast water dissociation centers and Mo atoms have strong adsorption properties toward hydrogen.[20] Therefore, the optimized Ni/Mo ratio (1.60 at% Mo) can provide modest hydrogen binding energy and enable effective chemisorption of H$_2$ atoms than that of an individual metal element.

In addition, HER activity of the NiMo (1.60 at% Mo) electrode prepared at different synthesis temperatures was examined, as shown in Figure 3c and Figure S15 (Supporting Information). Clearly, the polarization curves show that the NiMo-65 sample displayed outstanding HER activity with an onset overpotential as low as 3 mV, which is comparable to the Pt-based catalysts.[21] Remarkably, the overpotentials recorded at current densities of 10 and 400 mA cm^{-2} for NiMo-65 electrode were extremely low

as 17 and 98 mV, respectively, which significantly outperformed the control Pt/C catalyst and the NiMo samples prepared at other temperatures (70–80 °C). A more detailed survey shows that the HER performance of NiMo-65 nanowire electrode outperforms the reported state-of-the-art Pt-free HER electrocatalysts, such as Ni$_4$Mo nanosheets (35 mV at 10 mA cm^{-2}),[6] N-NiCo$_2$S$_4$ (28 mV at 10 mA cm^{-2}),[22] Ni (Cu)/NF pyramid arrays (27 mV at 10 mA cm^{-2}),[23] and NiMo nanowires (40 mV at 10 mA cm^{-2})[3a] (Table S3, Supporting Information). Moreover, the graphical comparison of our catalyst with other recently reported Pt-free catalysts in 1.0 M KOH at overpotential of 10 and 100 mA cm^{-2} is plotted in Figure 3e, showing excellent performance of NiMo-65 nanowire array electrode. However, LSV curves recorded for NiMo electrodes fabricated at temperature less than 65 °C show dramatic decrease in catalytic activity (Figure S16, Supporting Information). For instance, the electrode prepared at 60 °C shows high overpotential of 75 mV recorded at 10 mA cm^{-2} and it became worse with gradual decrease in synthesis temperature, due to poor growth kinetics and morphological control at low synthesis temperatures (Figure S3, Supporting Information). Furthermore, to verify the superiority of NiMo-65, we also tested NiMo electrodes prepared at 65 °C with different Mo content, which confirms again that higher percentage of Mo reduces the electrochemical activity (Figure S17, Supporting Information).

The superior HER activity for NiMo-65 can be attributed to the vertically assembled structure of nanowire arrays, high surface curvature, abundant edges/step sites, surface defects, as well as optimized Mo concentration. Among these parameters, the optimized Mo incorporation is especially conducive to modify the electronic structure through introducing strain induced by lattice mismatch (Table S2, Supporting Information) and thus optimize the hydrogen adsorption energy by forming $MoNi_4$ phase in NiMo alloy. In addition, due to the lattice expansion (d-band shift) of surface atoms as evident from Figure 2a, the intrinsic activity of metallic catalyst improves significantly as illustrated in Figure 3f.[24] Thus, $MoNi_4$ phase present in NiMo alloy and surface defective sites serve as active electrocatalytic sites. These results demonstrate that the excellent HER activity originates from collective contribution of both phase and surface defects.

In order to further investigate the rate determining reaction for HER, the derived Tafel plots of prepared electrodes after linear fitting of the polarization curves are shown in Figure 3b,d. As expected, NiMo-65 shows a small Tafel slope of 28 mV dec^{-1}, which is much lower than that of other electrodes and commercial available Pt/C. The smaller value of Tafel slope suggests that recombination reaction ($2H_{ads} \rightarrow H_2$) following the Volmer–Tafel mechanism is the rate limiting process.[25] The smaller Tafel slope can be ascribed to the increased number of active sites and fast gas bubbling at the electrode surface. The exchange current density of NiMo-65, which suggests the inherent HER activity of the electrode, was also calculated by extrapolating the Tafel plot to 0 V. The result shows that the exchange current density of NiMo-65 is significantly larger than those of other electrodes, as shown in **Figure 4**a and Figure S16c (Supporting Information).

To explore the details of the improved electrocatalytic activity, electrochemical active surface area (ECSA) of various electrodes was measured by using the cycling voltammetry technique to analyze the double-layer capacitance (C_{dl}) (Figure S18, Supporting Information). The increased number of active sites for NiMo-65 was confirmed by the higher C_{dl} (180 mF) value than other electrode samples, suggesting superior HER activity (Figure 4b). Furthermore, to confirm the influence of ECSA toward HER activity, specific current densities of the fabricated electrodes were calculated by normalizing the current densities with the corresponding ECSA (Figure S19, Supporting Information). These results show that NiMo-65 electrode displays much higher specific current densities than other electrodes, which demonstrates that this electrode is intrinsically more active. The electrochemical impedance spectroscopy (EIS) analysis was performed to investigate electrode kinetics from 100 kHz to 0.1 Hz at 50 mV overpotential versus RHE. The Nyquist plots show that the charge transfer resistance of NiMo-65 was the lowest among all electrodes. This result supports that the prepared 3D electrode provides fast charge transport, leading to faster HER kinetics and improved catalytic performance (Figure 4c).

Long-term stability is another critical parameter that counts for a practical HER electrode. Figure 4d shows the long-term chronoamperometry stability performance of the as-prepared NiMo electrodes synthesized at different temperatures, recorded at a constant overpotential of 50 mV. Notably, NiMo-65 electrode exhibits a stable and high current density of 23 mA cm^{-2} after electrolyzing for 24 h as compared to the other electrodes, implying excellent mechanical robustness and mass transport properties. The inset in Figure 4d shows the SEM image of NiMo-65 after stability test. Moreover, the structural stability was investigated by TEM analysis after stability test which
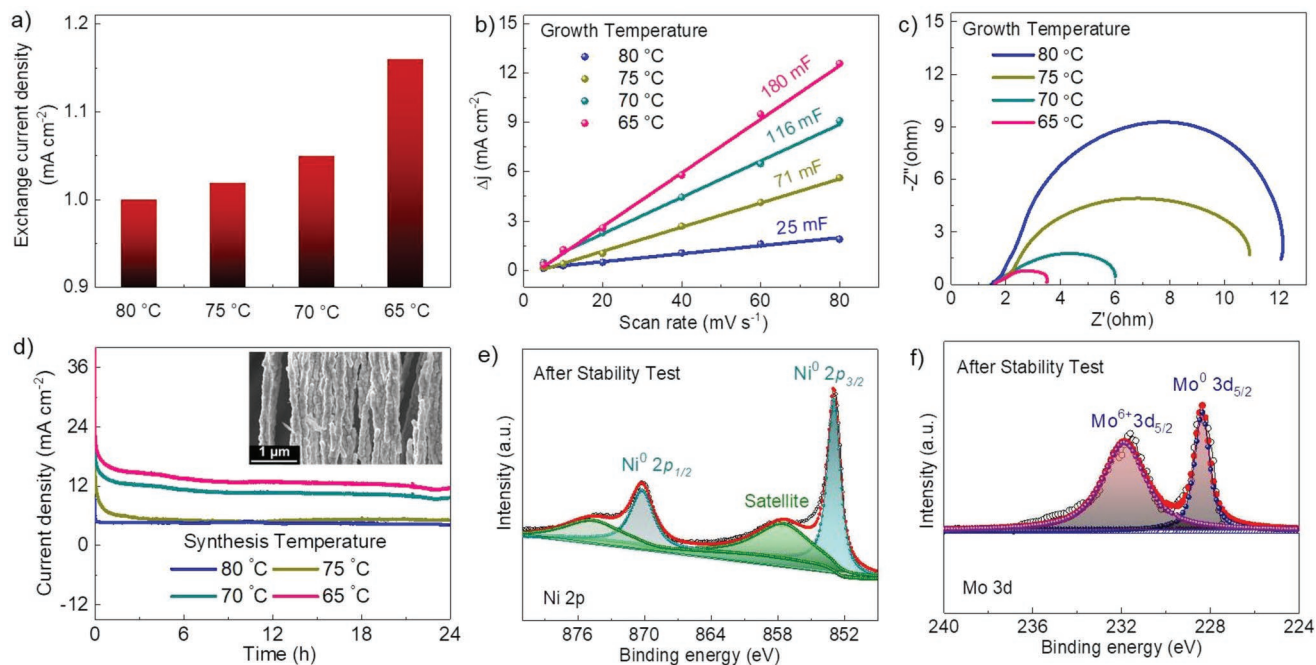
Figure 4. Electrochemical results of NiMo (1.60 at% Mo) electrode prepared at various synthesis temperatures. a) Exchange current densities. b) Capacitive current as a function of scan rates. c) Nyquist plots of different NiMo electrodes. d) Long-term cycling stability performance, where the inset is the SEM image of NiMo-65 electrode after cycling. e,f) XPS spectra of NiMo-65 after long-term stability test: Ni 2p and Mo 3d.

indicates that the morphology of nanowire arrays can be preserved, suggesting the stable structural characteristic of the prepared electrode (Figure S20, Supporting Information). The XPS study also confirms that the structure of NiMo-65 can be well maintained after stability testing, suggesting its superior chemical stability (Figure 4e,f).

Here, we can attribute the outstanding HER performance of NiMo electrode to the higher adsorption ability of NiMo alloy, kinked surface, induced defects, and hierarchical geometry of the nanowire arrays. It has been reported that the synergistic effects between Ni and Mo promote the adsorption ability due to the higher adsorption energy of Mo atoms.[26] Specifically, the incorporation of Mo tends to increase the bond length of Ni atom with its adjacent Ni; however, it decreases in Ni–Mo and thus, the d-band of Mo downshifts toward the Fermi level.[27] This downshift modulates the Mo–H binding energy and promotes the recombination of H_{ads} atoms to hydrogen molecule.[28] Another reason for such excellent HER performance is the abundant amount of kinked surfaces which provide additional sites to adsorbed atoms for excellent catalytic activity.[29] In addition, the synergistic effects between NiMo alloy and metallic nickel modulate the electronic states to improve the electrical conductivity of the catalyst and H-spillover ability of the electrode.[30] Defect engineering is another figure of merit to tune the catalytic activity in low-dimensional materials by distorting the atomic arrangement on the catalyst surface.[24] Finally, high surface area, well-aligned and reticular geometry of nanowire arrays contribute to boost the active sites and stimulate the generation of gas bubbles from the electrode surface. Therefore, these morphological features have potential to improve the charge transfer process due to the enhancement of the electrode utilization and contribute for the improvement of catalytic activity.

3. Conclusion and Outlook

In summary, 3D NiMo solid solution nanowire array electrodes with well-controlled morphology and unique electronic/structural regulations were successfully fabricated via a facile and effective magnetic field assisted growth method. Experimental results demonstrate that the fabricated NiMo-65 electrode exhibits superior HER activity and prominent long-term stability, which is highly comparable to the Pt-based control sample and superior to most state-of-the-art Pt-free catalysts. More importantly, the small Tafel slope indicates that NiMo electrode can lower the kinetic energy barrier for Volmer step and enhance the HER activity in alkaline conditions. Notably, at optimized synthesis temperature, the nanowire arrays can grow up to very long, which provide ample amount of active sites for better charge transfer and efficiently lower the contact resistance during the reaction. Both the rational design and fundamental understanding of HER kinetics of NiMo-based electrode provide a promising substitute to Pt-based catalysts.

It is understandable that elongating the nanowires can increase the number of active sites to enhance catalytic performance. But too long size is not conducive to withstanding the stress tolerance toward H_2 bubbling at high working current. Further investigations on length, diameter, elemental composition, and crystalline property on the electrocatalytic performance, especially at even larger current densities are still undergoing. We also note that by introducing more different element species into the nanowires can potentially further elevate catalytic performance. Finally, we can envisage that our strategy here can provide a platform technology to explore a large variety of earth-abundant elements for diverse electrocatalytic applications beyond HER, such as electrochemical metal-air batteries and fuel cells.

4. Experimental Section

Chemicals and Substrate Preparation: Nickel chloride hexahydrate ($NiCl_2 \cdot 6H_2O$), sodium molybdate dehydrate ($Na_2MoO_4 \cdot 2H_2O$), palladium chloride ($PdCl_2$), hydrazine monohydrate ($N_2H_4 \cdot H_2O$), trisodium citrate dihydrate ($Na_3C_6H_5O \cdot 2H_2O$), and potassium hydroxide (KOH) were all purchased from Alfa Aeser. All chemicals were used as received. Titanium sheet (99% pure, 0.5 mm thickness) was used as a substrate. First, the Ti foil was successively washed ultrasonically by ethanol and deionized water. Second, one piece of Ti foil was immersed into Pd plating bath to obtain a thin layer of Pd on Ti foil in an aqueous solution containing 0.23 M $PdCl_2$, 0.4 vol% HCl, 30 vol% ammonia solution, and 5×10^{-3} M hydrazine for 30 min. After that the plated Ti foil was thoroughly washed with deionized water and dried.

Fabrication of NiMo Nanowire Arrays: NiMo solid solution nanowire arrays were fabricated by deposition on Ti foil by using magnetic field assisted growth process. Deposition was performed in an aqueous mixture of $NiCl_2 \cdot 6H_2O$, $Na_3C_6H_5O_7 \cdot 2H_2O$, and $Na_2MoO_4 \cdot 2H_2O$ with 95:05, 90:10, and 80:20 wt% of Ni:Mo salts. Initially, NiMo electrode was prepared using 95:05 wt% of Ni:Mo salts, respectively, in 100 mL aqueous solution and pH value of the solution was adjusted to 12 using KOH. Later, an equal amount of $N_2H_4 \cdot H_2O$ with controlled pH value of 12 was mixed in the initial solution as a reducing agent. All experiments were performed in an external magnetic field (0.1 T) for an hour without stirring. During synthesis, initially Ni and Mo are primarily reduced into nanoparticle nucleus due to strong reducibility of hydrazine hydrate. Afterward, the magnetic effect between the formed nanoparticles will induce them to join together and applied magnetic field will tend to align them in the direction of applied field and coalesce into nanowire. The nanowire arrays were prepared on pretreated Ti foil which was kept vertically in the preheated solution at 80 °C. Subsequently, the fabricated nanowire arrays were washed by ethanol and deionized water and dried at 60 °C. The other NiMo electrodes were fabricated in the similar trend with particular compositions (90:10, and 80:20 wt%) and temperatures (80–40 °C).

Structural Characterization: To analyze phase and crystal structure, XRD patterns were recorded by using Cu Kα radiation by X-ray diffractometer (Bruker DS RINT2000/PC). SEM (HITACH S4800) was operated at 5 kV to analyze the morphology of the prepared electrodes. Furthermore, TEM and HRTEM images were captured on TEM (JEM 2100F) at an acceleration voltage of 200 kV. XPS (ESCALABSB 250 Xi) spectra were recorded to analyze the surface species and their chemical states. The elemental concentration of samples was analyzed by inductively coupled plasma atomic emission spectroscopy (ICP-AES-FHM22). The surface areas of the prepared electrodes were measured by specific surface area analyzer (MDTC-EQ-M03-01).

Electrochemical Measurement: The electrochemical measurements were performed with a CHI 660E electrochemical analyzer at room temperature. NiMo nanowire array electrode was directly used as working electrode, while Pt/C electrode was prepared by dispersion of Pt/C powder into mixture of water/ethanol (4:1) and 10 μL of 5 wt% Nafion solution, followed by ultrasonication for 0.5 h. Later on, certain amount of catalyst solution was drop-casted onto a glassy carbon electrode with a diameter of 3 mm. After being dried the electrode was used as working electrode for the electrochemical measurements. The electrode was put

in solutions without rotation or stirring of solution. The as-prepared electrode, graphite rod, and Ag/AgCl electrode with the electrolyte of 3 M KCL solution were used as the working electrode, counter electrode, and reference electrode, respectively. All polarization curves were recorded after iR compensation in a three-electrode configuration system. All tests were carried out in 1 M KOH solution and potential was referred versus RHE by $E_{RHE} = E_{Ag/AgCl} + 0.197 + 0.0591 \times pH$. The solution was bubbled by N_2 gas for 5 min prior to the HER. The mass loading amount of catalysts was estimated to be about 2 mg cm^{-2}. Subsequently, polarization curves were obtained by linear sweep voltammetry method with a scan rate of 5 mV s^{-1} for HER. The electrochemical impedance spectra of the fabricated electrodes were carried out by AC impedance spectroscopy under the frequency range from 100 kHz to 0.1 Hz at 50 mV overpotential versus RHE. Furthermore, cyclic voltammetry was carried out in 1 M KOH at various scan rates (5, 10, 20, 40, 60, and 80 mV s^{-1}) to investigate the electrochemical double-layer capacitance of all prepared electrodes.

Supporting Information

Supporting Information is available from the Wiley Online Library or from the author.

Acknowledgements

Conflict of Interest

The authors declare no conflict of interest.

Keywords

[1] a) L. Schlapbach, A. Zuttel, *Nature* **2001**, *414*, 353; b) L. Schlapbach, *Nature* **2009**, *460*, 809.

[2] Y. L. Sun, M. Delucchi, J. Ogden, *Int. J. Hydrogen Energy* **2011**, *36*, 11116.

[3] a) M. Fang, W. Gao, G. Dong, Z. Xia, S. Yip, Y. Qin, Y. Qu, J. Ho, *Nano Energy* **2016**, *27*, 247; b) J. Lu, T. Xiong, W. Zhou, L. Yang, Z. Tang, S. Chen, *ACS Appl. Mater. Interfaces* **2016**, *8*, 5065.

[4] J. Zhang, T. Wang, P. Liu, Z. Liao, S. Liu, X. Zhuang, M. Chen, E. Zschech, X. Feng, *Nat. Commun.* **2017**, *8*, 15437.

[5] B. Ye, B. Jeong, M. Lee, H.-D. Kim, J. M. Baik, *Adv. Mater. Technol.* **2019**, *4*, 1800462.

[6] Q. Zhang, P. Li, D. Zhou, Z. Chang, Y. Kuang, X. Sun, *Small* **2017**, *13*, 1701648.

[7] J. Hou, Y. Wu, S. Cao, Y. Sun, L. Sun, *Small* **2017**, *13*, 1702018.

[8] a) J. N. Tiwari, S. Sultan, C. W. Myung, T. Yoon, N. Li, M. Ha, A. M. Harzandi, H. J. Park, D. Y. Kim, S. S. Chandrasekaran, W. G. Lee, V. Vij, H. Kang, T. J. Shin, H. S. Shin, G. Lee, Z. Lee, K. S. Kim, *Nat. Energy* **2018**, *3*, 773; b) Y. Xie, J. Cai, Y. Wu, Y. Zang, X. Zheng, J. Ye, P. Cui, S. Niu, Y. Liu, J. Zhu, X. Liu, G. Wang, Y. Qian, *Adv. Mater.* **2019**, *31*, 1807780.

[9] L. Xiao, S. Zhang, J. Pan, C. Yang, M. He, L. Zhuang, J. Lu, *Energy Environ. Sci.* **2012**, *5*, 7869.

[10] H. Huang, J.-R. Li, K. Wang, T. Han, M. Tong, L. Li, Y. Xie, Q. Yang, D. Liu, C. Zhong, *Nat. Commun.* **2015**, *6*, 8847.

[11] H. Sun, J. Zhu, D. Baumann, L. Peng, Y. Xu, I. Shakir, Y. Huang, X. Duan, *Nat. Rev. Mater.* **2019**, *4*, 45.

[12] a) Q. Gao, W. Zhang, Z. Shi, L. Yang, Y. Tang, *Adv. Mater.* **2018**, 1802880; b) J. Li, G. Zheng, *Adv. Sci.* **2017**, *4*, 1600380.

[13] S. Peng, L. Li, H. B. Wu, S. Madhavi, X. W. Lou, *Adv. Energy Mater.* **2015**, *5*, 1401172.

[14] B. Ni, X. Wang, *Adv. Sci.* **2015**, *2*, 1500085.

[15] a) D. Gao, J. Guo, X. Cui, L. Yang, Y. Yang, H. He, P. Xiao, Y. Zhang, *ACS Appl. Mater. Interfaces* **2017**, *9*, 2240; b) H. Xu, J. Wei, K. Zhang, Y. Shiraishi, Y. Du, *ACS Appl. Mater. Interfaces* **2018**, *10*, 29647.

[16] X. Yan, L. Tian, X. Chen, *J. Power Sources* **2015**, *300*, 336.

[17] X. Wang, R. Su, H. Aslan, J. Kibsgaard, S. Wendt, L. Meng, M. Dong, Y. Huang, F. Besenbacher, *Nano Energy* **2015**, *12*, 9.

[18] L. Ji, J. Wang, L. Guo, Z. Chen, *J. Mater. Chem. A* **2017**, *5*, 5178.

[19] J. R. McKone, B. F. Sadtler, C. A. Werlang, N. S. Lewis, H. B. Gray, *ACS Catal.* **2013**, *3*, 166.

[20] a) R. Subbaraman, D. Tripkovic, K. C. Chang, D. Strmcnik, A. P. Paulikas, P. Hirunsit, M. Chan, J. Greeley, V. Stamenkovic, N. M. Markovic, *Nat. Mater.* **2012**, *11*, 550; b) J. W. D. Ng, M. García-Melchor, M. Bajdich, P. Chakthranont, C. Kirk, A. Vojvodic, T. F. Jaramillo, *Nat. Energy* **2016**, *1*, 16053.

[21] Z. Zhang, G. Liu, X. Cui, B. Chen, Y. Zhu, Y. Gong, F. Saleem, S. Xi, Y. Du, A. Borgna, Z. Lai, Q. Zhang, B. Li, Y. Zong, Y. Han, L. Gu, H. Zhang, *Adv. Mater.* **2018**, *30*, 1801741.

[22] Y. Wu, X. Liu, D. Han, X. Song, L. Shi, Y. Song, S. Niu, Y. Xie, J. Cai, S. Wu, J. Kang, *Nat. Commun.* **2018**, *9*, 1425.

[23] Q. Sun, Y. Dong, Z. Wang, S. Yin, C. Zhao, *Small* **2018**, *14*, 1704137.

[24] D. Voiry, H. S. Shin, K. P. Loh, M. Chhowalla, *Nat. Rev. Chem.* **2018**, *2*, 0105.

[25] J. Mahmood, F. Li, S. M. Jung, M. S. Okyay, I. Ahmad, S. J. Kim, N. Park, H. Y. Jeong, J. B. Baek, *Nat. Nanotechnol.* **2017**, *12*, 441.

[26] M. Fang, W. Gao, G. Dong, Z. Xia, S. Yip, Y. Qin, Y. Qu, J. C. Ho, *Nano Energy* **2016**, *27*, 247.

[27] P. A. Ferrin, S. Kandoi, J. Zhang, R. Adzic, M. Mavrikakis, *J. Phys. Chem. C* **2009**, *113*, 1411.

[28] W. F. Chen, K. Sasaki, C. Ma, A. I. Frenkel, N. Marinkovic, J. T. Muckerman, Y. Zhu, R. R. Adzic, *Angew. Chem., Int. Ed.* **2012**, *51*, 6131.

[29] R. L. Arevalo, S. M. Aspera, M. C. S. Escaño, H. Nakanishi, H. Kasai, *Sci. Rep.* **2017**, *7*, 13963.

[30] Y.-Y. Chen, Y. Zhang, X. Zhang, T. Tang, H. Luo, S. Niu, Z.-H. Dai, L.-J. Wan, J.-S. Hu, *Adv. Mater.* **2017**, *29*, 1703311.